Volumetric curvature attributes add value to 3D seismic data interpretation

Satinder Chopra, Arcis Corporation, Calgary, Canada
Kurt J. Marfurt, University of Houston, USA

Horizon-based curvature attributes have been used in seismic data interpretation for predicting fractures since 1994 when Lisle demonstrated the correlation of curvature values to fractures measured on an outcrop. Different measures of curvature (such as Gaussian, strike, and dip) have been shown by different workers to be highly correlated with fractures, and many more applications are also possible. By definition, all such applications need the interpretation of a seismic horizon, which may be simple if data quality is good and the horizon of interest corresponds to a prominent impedance contrast.

In contrast, horizons picked on noisy seismic data contaminated by back-scattered noise and/or acquisition footprint, or picked through regions where no consistent impedance contrast exists, can lead to inferior curvature measures. One partial solution to noisy picks is to run a spatial filter over them, taking care to remove the noise yet retain the geometric detail.

A significant advance in the area of curvature attributes is the volumetric estimation of curvature at different wavelengths introduced by Al-Dossary and Marfurt (2006). This volumetric estimation of curvature alleviates the need for picking horizons for regions in which no continuous surface exists. This paper reports our investigations into both horizon-based and volumetric curvature attribute applications.

A key point is that, even after careful spatial filtering, horizon-based curvature estimates may still suffer from artifacts. Conversely, curvature attribute values extracted from curvature attribute volumes along the same horizons yield displays free of artifacts and make more geologic sense.

Attributes and structure-oriented filtering. The purpose of filtering along seismic events is to remove noise and enhance lateral continuity. This can be done by differentiating between the dip/azimuth of the reflector and that of the underlying noise. Once the dip/azimuth has been estimated, a filter can enhance signal along the reflector, much as interpreters do with time/structure and amplitude extraction maps using interpretation workstation software. The familiar filters are the mean, median, and trimmed mean. While
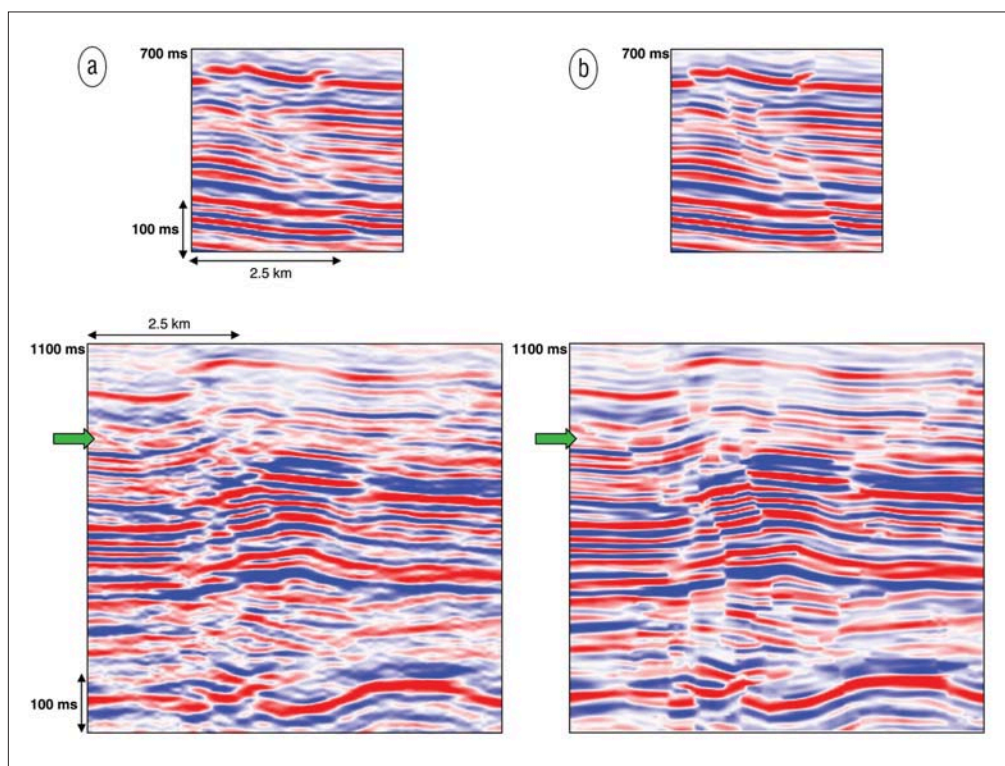

Figure 1. Two segments of a seismic section (a) before and (b) after the application of structure-oriented pc filtering from a 3D seismic volume from Alberta, Canada. Notice the cleaner background and focused amplitudes of the seismic reflections after pc filtering as well as the preserved fault edges.

The subject of this article is covered more extensively in SEG's newest publication, *Seismic Attributes for Prospect Identification and Reservoir Characterization*, by Chopra and Marfurt. This 456-page book introduces the physical basis, mathematical implementation, and geologic expression of modern volumetric attributes including coherence, dip/azimuth, curvature, amplitude gradients, seismic textures, and spectral decomposition. Available now at *www.seg.org*.
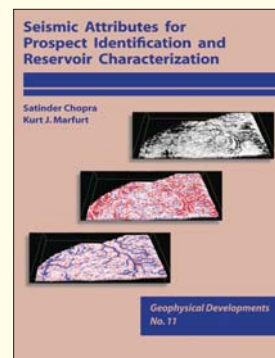
these do a good job enhancing the signal-to-noise ratio of the data, they smear faults.

Hoecker and Fehmers (2002) address this problem by using an "anisotropic diffusion" smoothing algorithm. The anisotropic part is so named because the smoothing takes place parallel to the reflector, while no smoothing takes place perpendicular to the reflector. Most important, no
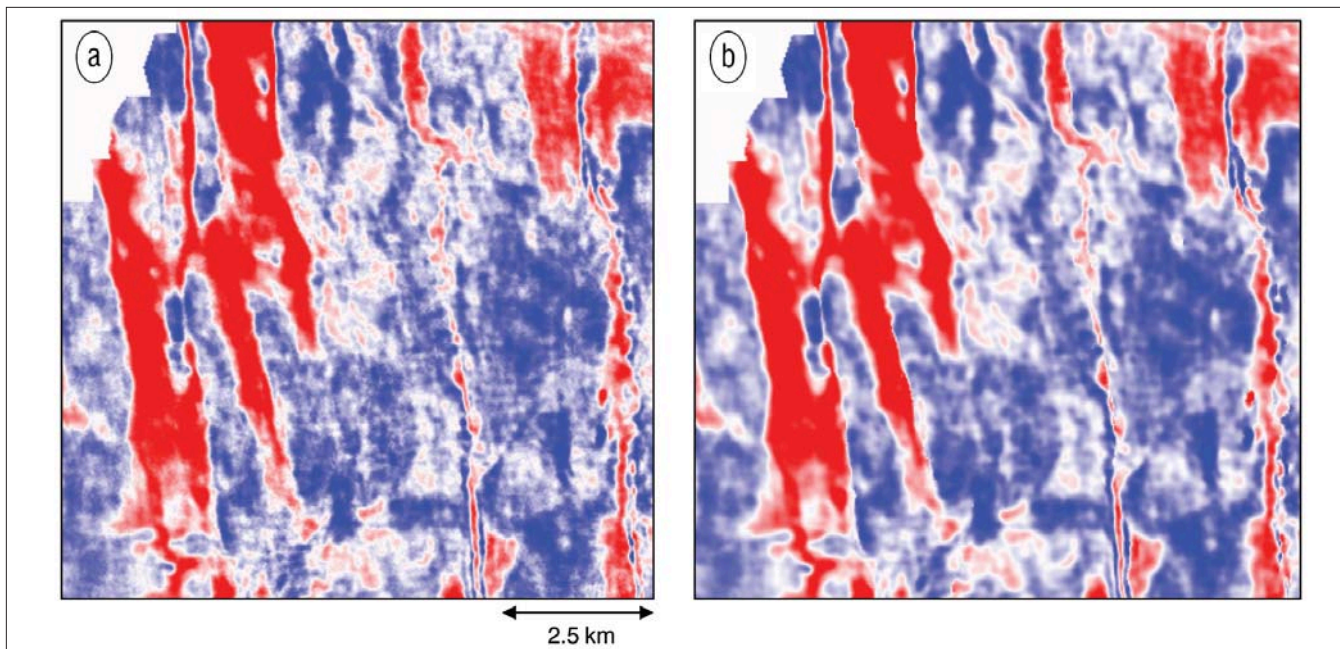
Figure 2. *Time slices (at 1232 ms) from the seismic volume generated (a) before and (b) after structure-oriented pc filtering of data, shown in Figure 1, but from a different portion of the survey. Notice the reduced background noise and focused edges of the features on these time slices after pc filtering.*
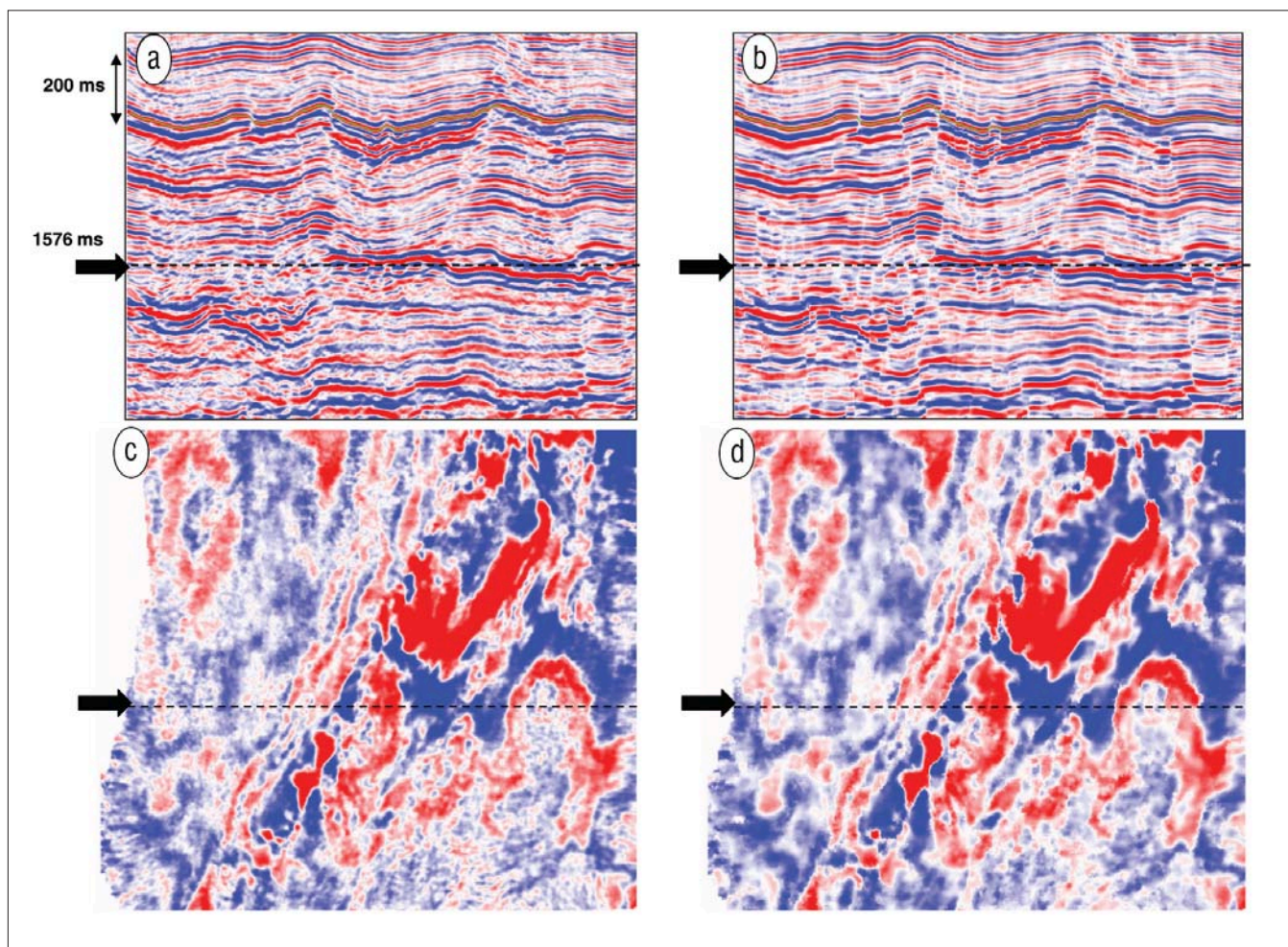

Figure 3. *Segment of a seismic section from a 3D seismic volume from northeastern British Columbia, Canada (a) before and (b) after application of structure-oriented pc filtering. Notice the cleaner background and focused amplitudes of the seismic reflections after pc filtering as well as the preserved fault edges. Time slices (at 1576 ms) from the seismic volume generated (c) before and (d) after pc filtering of the data shown in Figures 3a and b. The position of the seismic lines shown above is indicated with dotted lines. Notice the reduced background noise and focused edges of the features on these time slices after pc filtering.*
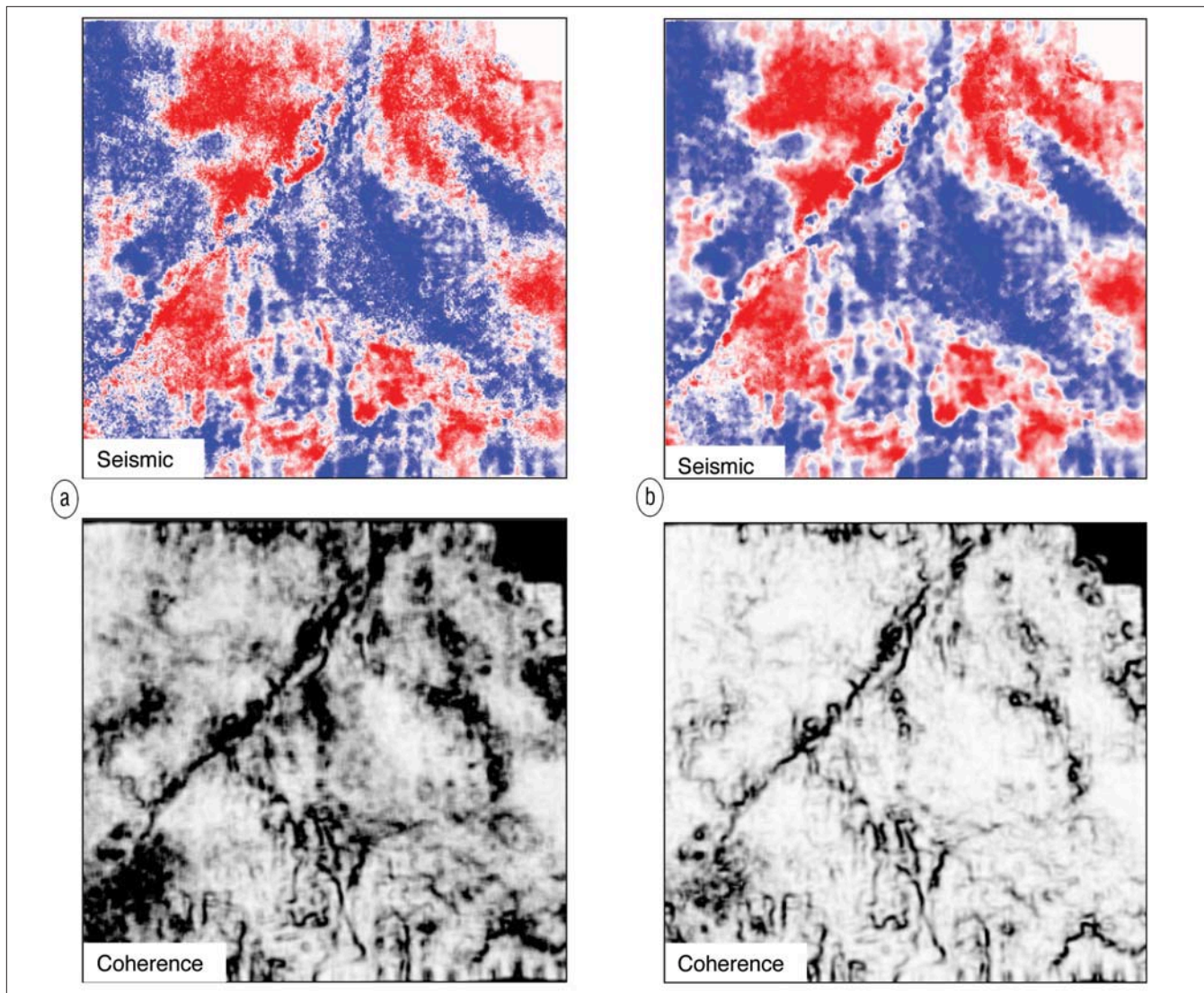
Figure 4. *Time slice from a 3D seismic volume from Alberta, Canada (a) before and (b) after structure-oriented pc filtering. The equivalent coherence attribute slices are shown in Figures 4c and d; notice that Figure 4d is a cleaner display with crisper features.*

Figure 5. *Fractional derivatives visualized as filters applied to the conventional first-derivative operator. The idealized derivative is proportional to the wavenumber (k) and inversely proportional to the wavelength (λ). The dotted line represents a filter applied to the derivative operator δ/δx that would perfectly reproduce δ/δx. Any numerical operator needs to go to zero at Nyquist, or λ=2Δx. We compensate for coarser sampling artifacts at 45° to the grid by tapering the derivative after λ=4Δx. The 0.80 derivative slightly enhances the long wavelength components, while the 0.25 derivative greatly enhances the long wavelength components. The filters are normalized such that the area under the filtered spectrum (the product of the filter times the idealized first derivative) is equal to 1.0.*
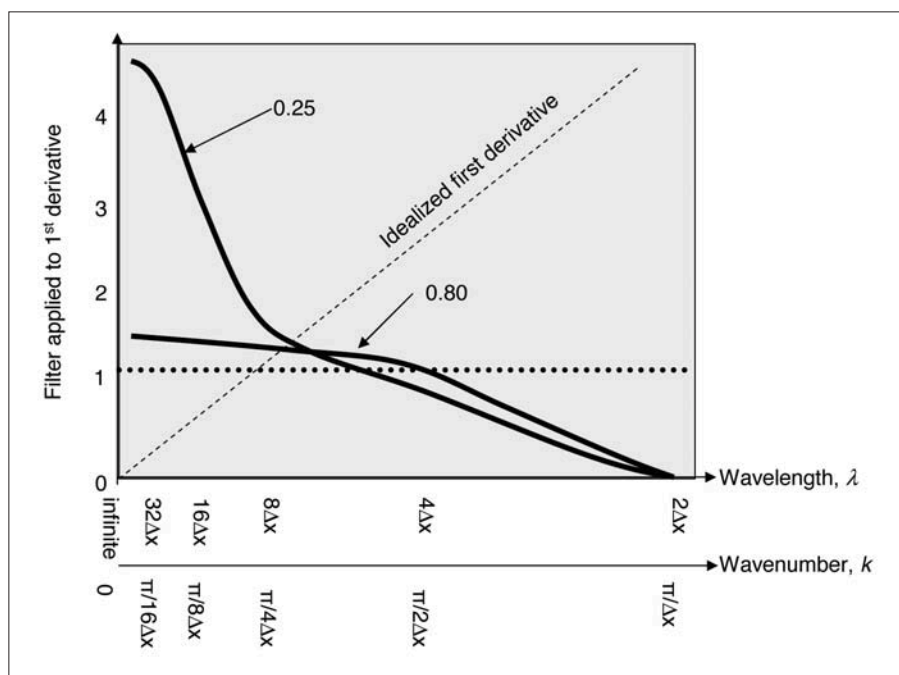
Figure 6. (a) Time surface from a 3D seismic data volume from Alberta, (b) most-positive curvature display for the time surface in (a), (c) most-negative curvature display for the time surface in (a). Arrows indicate some artifacts on the attribute slices.
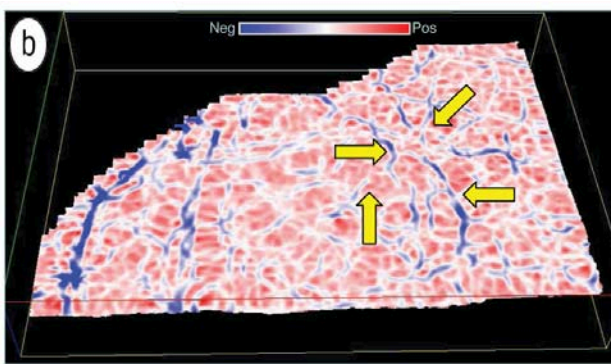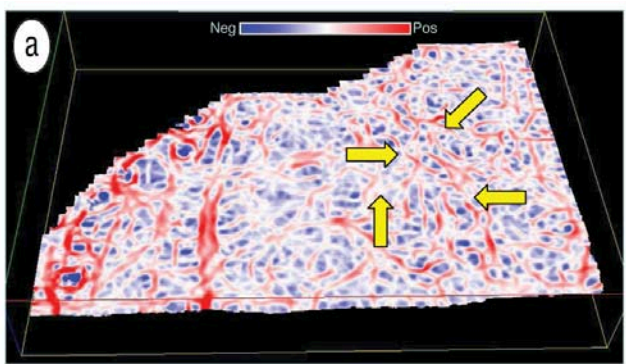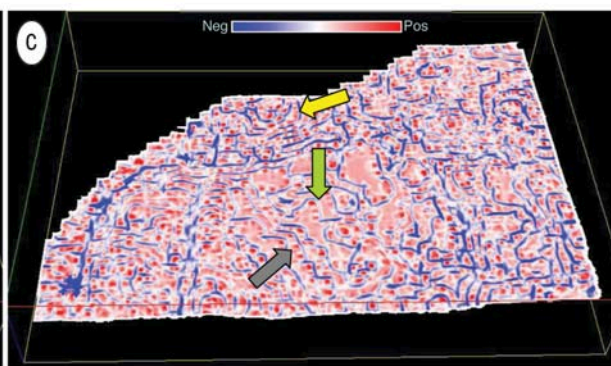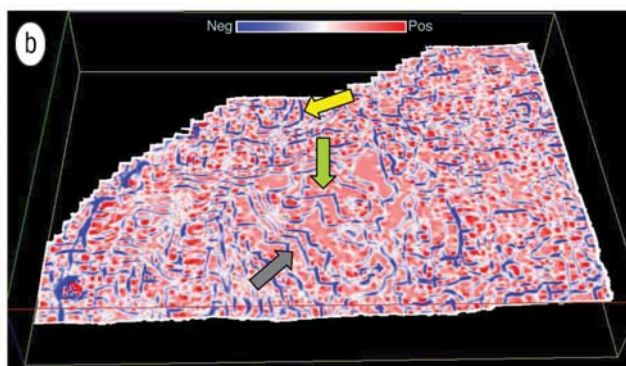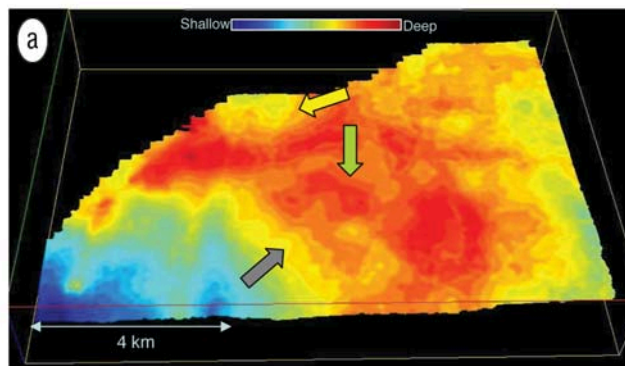

Figure 7. (a) Most-positive curvature display extracted from the attribute volume along the time surface in Figure 6a, (b) most-negative curvature display extracted from the attribute volume along the time surface in Figure 6a. Artifacts are suppressed on these slices.

smoothing takes place if a discontinuity is detected, thereby preserving the appearance of major faults and stratigraphic edges. Luo et al.'s (2002) edge-preserved filtering proposed a competing method that uses a multiwindow (Kuwahara) filter to address the same problem. Both approaches use a mean or median filter applied to data values that fall within a spatial analysis window with a thickness of one sample.

Marfurt (2006) describes a multiwindow (Kuwahara) principal component filter that uses a vertical window of data samples to compute the waveform that best represents the seismic data in the spatial analysis window. Seismic processors may be more familiar with the principal component filter as the equivalent Kohonen-Loeve (or simply KL) filter. In this paper, we use 99 nine-trace, ±10-ms (11-sample) analysis windows parallel to the dip/azimuth that contains the analysis point of interest. We then apply our principal component (pc) filter to the analysis point using the window that contains the most coherent data. Because it uses (for our examples 11 times) more data, the pc filter in general produces significantly better results than the corresponding mean filter. We advise the hopeful reader that there is no such thing as a "silver bullet" in seismic data

processing. If the data are contaminated by high-amplitude spikes, then a median, alpha-trim mean, or other nonlinear filter will provide superior results. Likewise the pc filter will preserve amplitude variations in coherent signal that may exacerbate acquisition geometry, whereas a mean filter will smooth them out.

Seismic data that have been pc filtered will in general have a higher signal-to-noise ratio, exhibit sharper discontinuities, and provide enhanced images of faults, fractures and stratigraphic features such as channels. Autotrackers tend to work much better on filtered data, providing continuous surfaces that stop at discontinuities. Attributes extracted from these data often yield more meaningful displays than those from unfiltered data; however, not all features of geologic interests appear as edges. Structure-oriented filtering will smooth out and therefore diminish the easily recognized "chaotic" textures associated with karst, mass-transport complexes, and hydrothermally altered dolomite.

Figure 1 shows the result of pc filtering on a 3D seismic data set from Alberta. Notice not only the overall cleaner look of the section after pc filtering, but also the sharpen-

Figure 8. (a) Time surface from a 3D seismic data volume from Alberta, and lines (b) AA' and (c) BB' through the seismic volume. The picked cyan horizon is displayed in Figure 6a. The green phantom horizon is 36 ms above the cyan horizon and cuts a sequence of channels, some of which are indicated by arrows in (c). Since the phantom horizon in (a) is simply a time-shifted version of that displayed in Figure 6a, it is not directly sensitive to the channels seen at this level on the seismic data in (b) and (c). Obviously, horizon-based curvature computed from a phantom horizon would produce images identical to those computed from the deeper horizon used to generate it.
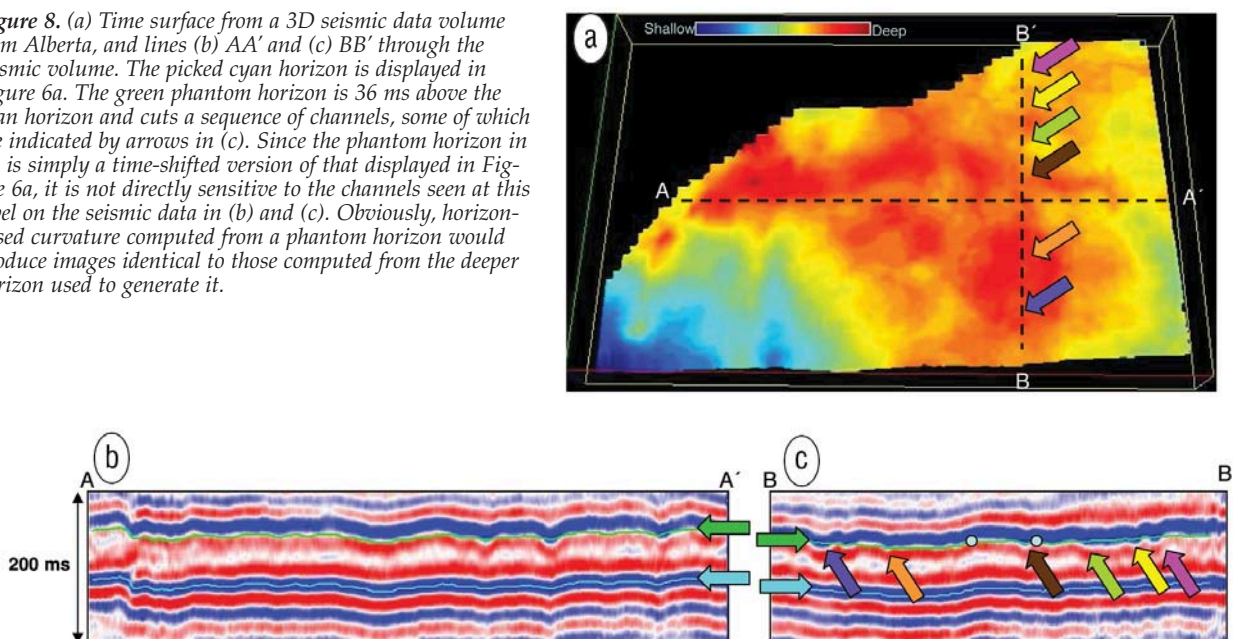

Figure 9. Phantom horizon slices through the (a) coherence, (b) most-positive curvature (long-wavelength), and (c) most-negative curvature (long-wavelength) volumes corresponding to the green horizon displayed in Figure 8. Channel edges are visible in coherence, the thalweg (or channel axis) on the most-negative curvature, and the channel flanks and levee complexes on the most-positive curvature. Arrows indicate channels seen on the seismic line BB' displayed in Figure 8c. Each of these images is mathematically independent of and complementary to the others.
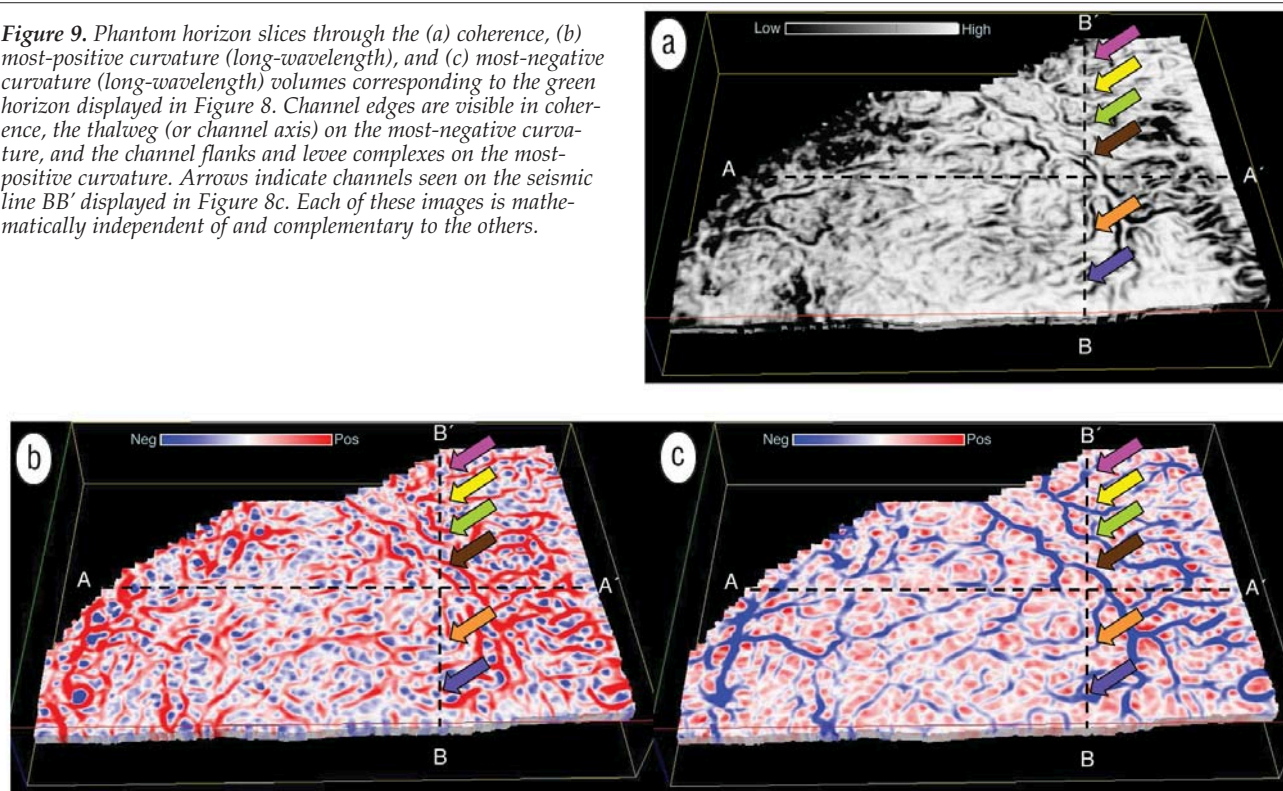
ing of the vertical faults. Figure 2, from a different part of the same survey, compares time slices before and after pc filtering; improved event focusing and reduced background noise levels after structure-oriented pc filtering are clearly evident. Figure 3 shows a similar comparison of an inline and a time slice before and after pc filtering.

Attributes computed from pc-filtered seismic data volumes. Attributes computed from seismic data having a good signal-to-noise ratio are bound to yield significantly more meaningful information. Figures 4a and b show seismic and coherence time slices before and after pc filtering. Not only

does the time slice in Figure 4b have better event definition and lower noise level, but the coherence derived from this data set shows sharper lineaments and less incoherent noise.

Geologic structures often exhibit curvature of different wavelengths, and curvature images having different wavelengths provide different perspectives of the same geology. Tight (short-wavelength) curvature often delineates details within intense, highly localized fracture systems. Broad (long-wavelength) curvature often enhances subtle flexures (on the scale of 100–200 traces, that are difficult to see in conventional seismic, but are often correlative to fracture zones that are below seismic resolution) and collapse features and
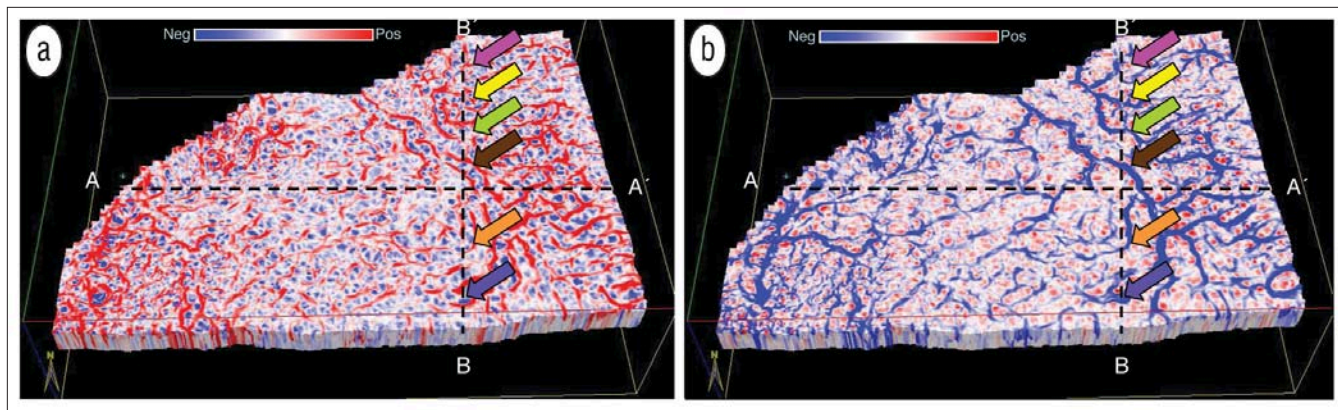
Figure 10. *Phantom horizon slices through the (a) most-positive curvature (short-wavelength) (b) most-negative curvature (short-wavelength) volumes corresponding to the green horizon displayed in Figure 8. Arrows indicate channels seen on the seismic line BB' displayed in Figure 8c.*
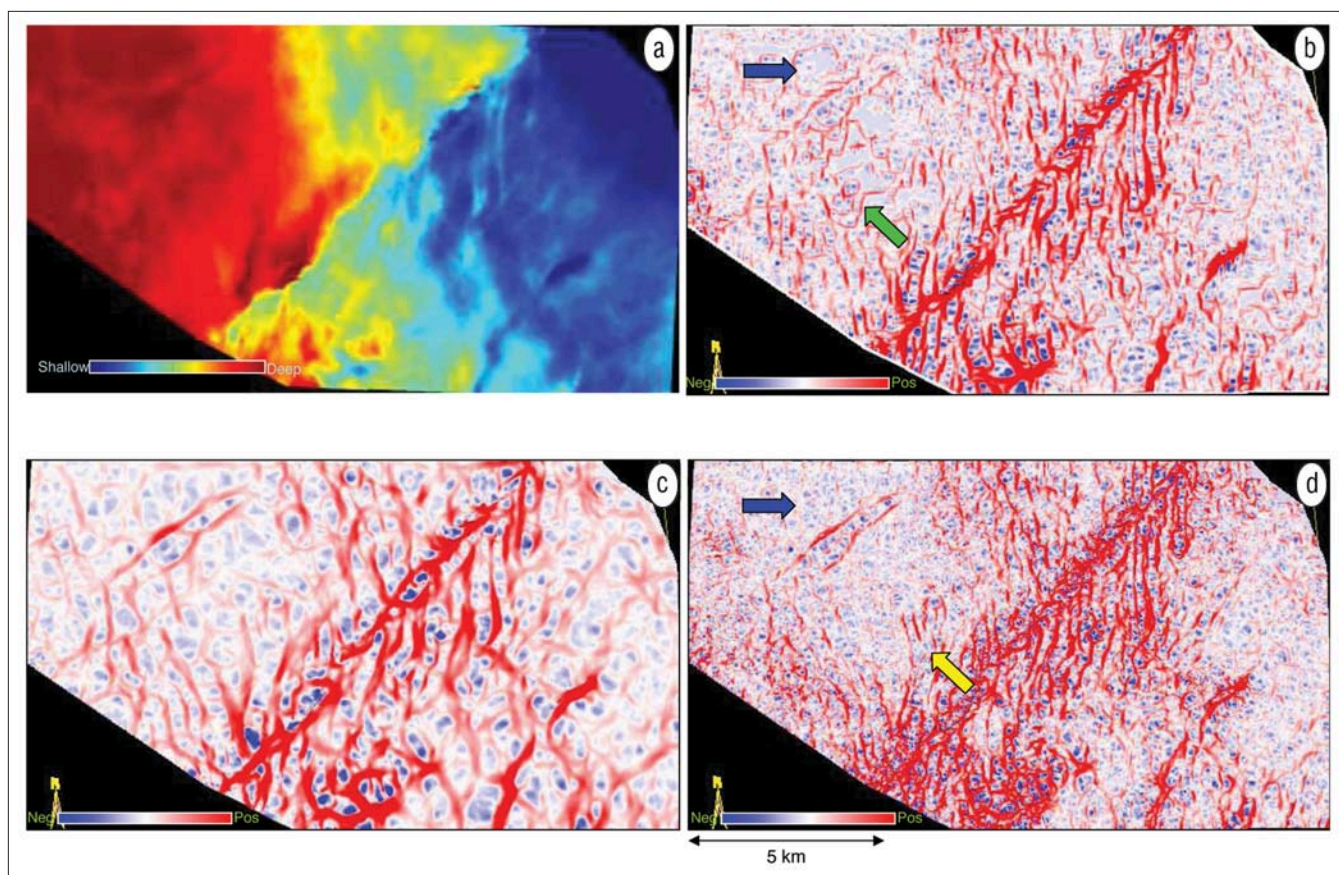

Figure 11. *(a) Time-structure map from a 3D seismic data volume from Alberta. Comparison of (b) horizon-based most-positive curvature and horizon slices through volumetric estimates of (c) most-positive curvature (long-wavelength), and (d) most-positive curvature (short-wavelength). Arrows indicate artifacts on the horizon-based display.*

diagenetic alterations that result in broader depressions.

Al-Dossary and Marfurt introduced a "fractional derivative" approach for volume computation of multispectral estimates of curvature. They define the fractional derivative as

$$F_\alpha\left(\frac{\partial u}{\partial x}\right) = -i(k_x)^\alpha F(u)$$

where the operator F denotes the Fourier transform, u is an inline or crossline component of reflector dip, and α is a fractional real number that typically ranges between 1 (giving the first derivative) and 0 (giving the Hilbert transform) of the dip. The nomenclature fractional derivative was borrowed from Cooper and Cowans (2003); however, an astute mathematician will note that the i is not in the parentheses.

In this manner we can interpret the preceding equation as simply a low-pass filter of the form $k_x^{(\alpha-1)}$ applied to a conventional first derivative. Figure 5 shows filters for values $\alpha=0.80$ and $\alpha=0.25$. Given the spectral response, particularly when multiplied by the spectral response of the derivative operator, we will call the resulting images "short-wavelength" and "long-wavelength" curvature in the figures that follow.

The space domain operators corresponding to different values of α mentioned above are convolved with the previously computed dip components estimated at every sample and trace within the seismic volume. In addition, the directional derivative is applied to a circular rather than linear window of traces, thereby avoiding a computational
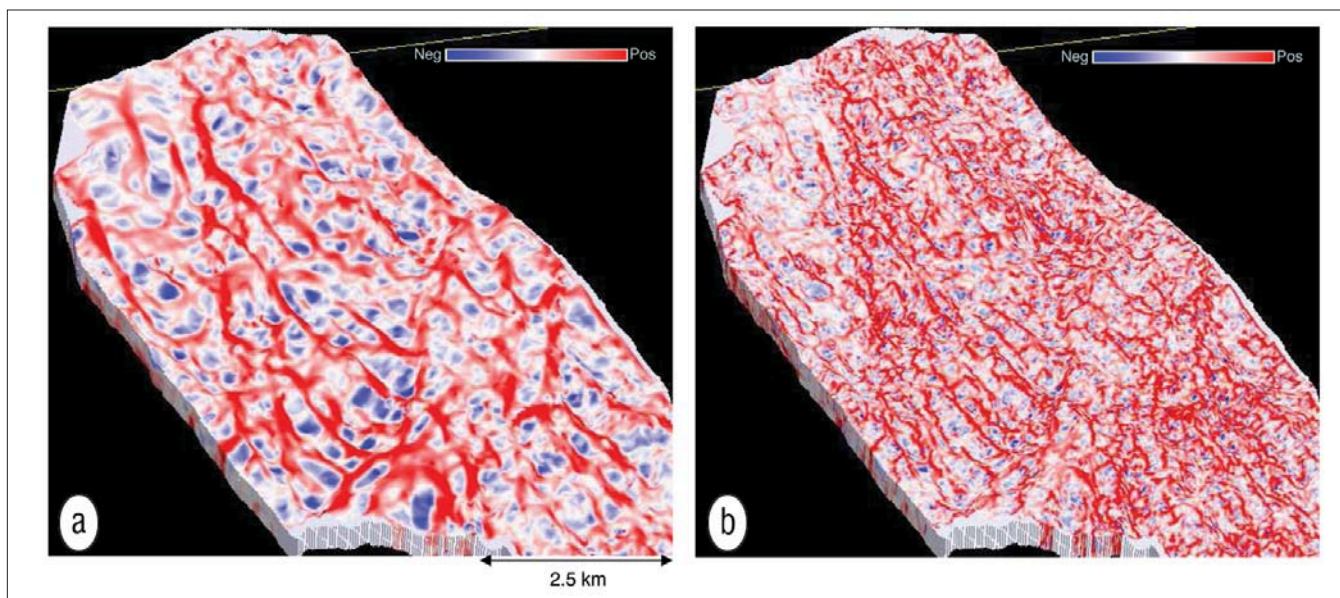
Figure 12. *Comparison of (a) long-wavelength and (b) short-wavelength most-positive curvature strat-cube displays from a 3D volume from Alberta. The finer detail in terms of fault/fracture lineaments could be useful for certain objectives. The upper surface is close to 1550 ms.*
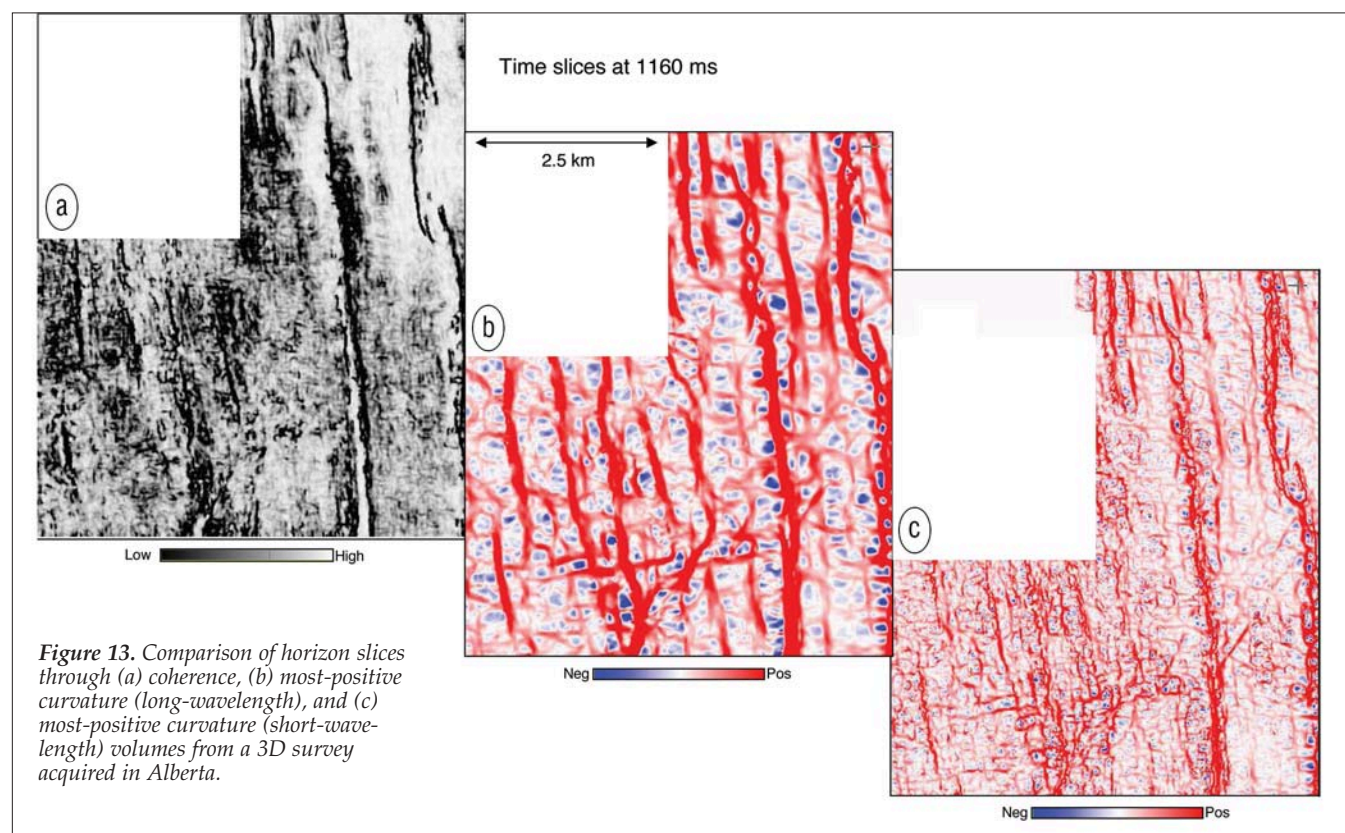

Figure 13. *Comparison of horizon slices through (a) coherence, (b) most-positive curvature (long-wavelength), and (c) most-positive curvature (short-wavelength) volumes from a 3D survey acquired in Alberta.*

bias associated with the acquisition axes. Lower values of α decrease the contribution of the high frequencies, thereby shifting the bandwidth toward longer wavelength.

Curvature images of differential compaction over channels. Figure 6a shows a time-structure map interpreted from a 3D seismic survey acquired in Alberta, Canada. This horizon was the nearest continuous event below a slightly shallower channel system of interest. We manually picked a grid of control lines, autotracked the horizon, and then applied a 3×3 mean filter to remove short wavelength jitter from the interpreted picks. Next, we computed the most-

positive and most-negative curvature directly from the autotracked and filtered horizon to generate the horizon-based curvature images in Figures 6a–c. Notice that both displays are contaminated by a time contour overprint, as indicated by the yellow, green and gray arrows. Such overprints are artifacts that do not make any geologic sense. We do not see any clear evidence of the channel system overlying this horizon.

Next, we computed volumetric estimates of most-positive and most-negative curvature corresponding to every sample in the seismic volume and displayed horizon slices through both attribute volumes (Figure 7). This is a short-
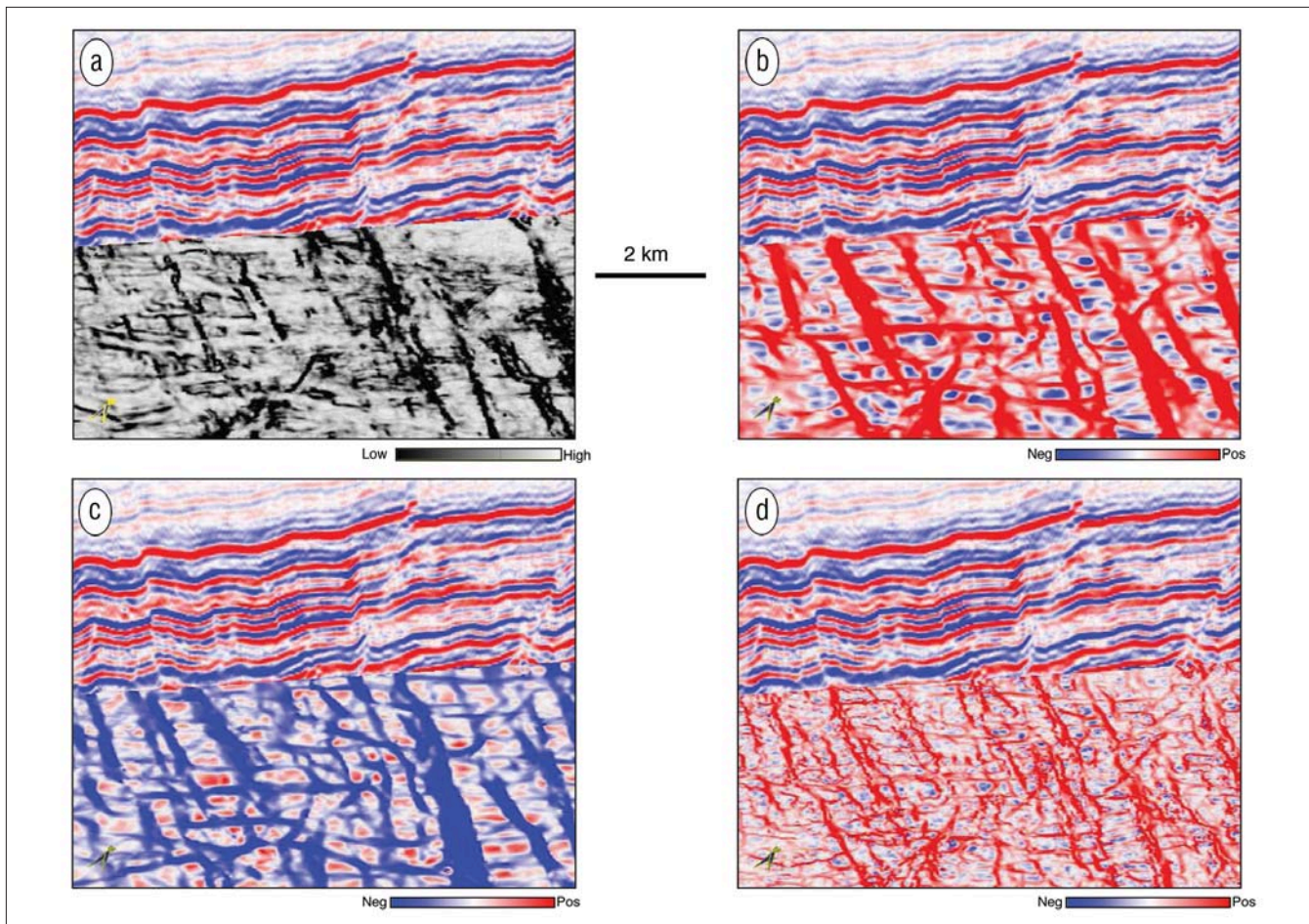
Figure 14. Enlargement of chair-displays in which the vertical display is an inline from the 3D seismic volume and the horizontal displays are time slices through (a) coherence, (b) most-positive curvature (long-wavelength), (c) most-negative curvature (long-wavelength), and (d) most-positive curvature (short-wavelength) volumes. The fault lineaments correlate with the upthrown and downthrown fault blocks on the vertical seismic sections.

wavelength estimate of curvature (α=0.25), and so the two displays are smoother than those shown in Figures 6b and c. Not only is Figure 7 free of the time contour artifacts in Figure 6b and c, but also depicts some limbs of a shallower channel system as indicated by the arrows. We interpret these deeper features to be the result of lateral velocity-thickness changes between the channel fill and the matrix through which the channels cut.

Figures 8b and c show vertical sections through the survey; Figures 6 and 7 were computed along the picked cyan horizon. We then computed a phantom horizon 36 ms above (green pick) the cyan pick. Since the phantom horizon is simply a vertical shift of the lower picks, it is insensitive to the channels indicated by the magenta, yellow, lime green, brown, orange, and blue arrows in Figure 8c. Figure 9 shows horizon slices through volumetric estimates of coherence, most-positive curvature, and most-negative curvature along this phantom horizon. Notice the clarity with which the channel system stands out, with the main limb running NW–SE and the other limbs showing the deltaic distribution on both sides. Because of differential compaction and the potential deposition of levees, the most-negative curvature highlights the channel axis or thalweg, while the most-positive curvature defines the flanks of the channels and potential levee and overbank deposits. The coherence images are complementary and are insensitive to differential compaction; rather, they highlight those areas of the channel flanks in which there is a lateral change in waveform.

The advantages of volumetric attributes are two-fold. First, as shown in Figures 6 and 7, volumetric attributes have higher signal-to-noise. Volumetric estimates of curvature are computed not from one picked seismic sample, but rather from a vertical window of seismic samples (in our case, 11 samples), such that they are statistically less sensitive to backscattered noise. Second, not every geologic feature that we wish to interpret falls along a horizon that can be interpreted, such as the channel system shown here. While we could interpolate horizon-based curvature computed above and below the channel system, such an interpolated image would be significantly less sensitive to the rapid geomorphological changes seen in the vertical section.

The volume curvature attributes displayed in Figure 9 are long-wavelength versions of curvature computed by using a value of α=0.25. Figure 10 shows a higher-resolution, shorter-wavelength version of curvature by using a value of α=0.80 as discussed in Figure 5. Notice the sharper patterns corresponding to the channel levees and the base of the different channel limbs.

Curvature images of faults and fractures. In addition to enhancing channel features, such displays could improve definition of subtle faults and fractures to help in the placement of horizontal wells. Figure 11a shows a time horizon depicting a positive NE–SW positive flexure cut by a dense system of NS trending faults and flexures. Figure 11b shows most-positive curvature computed from the smoothed
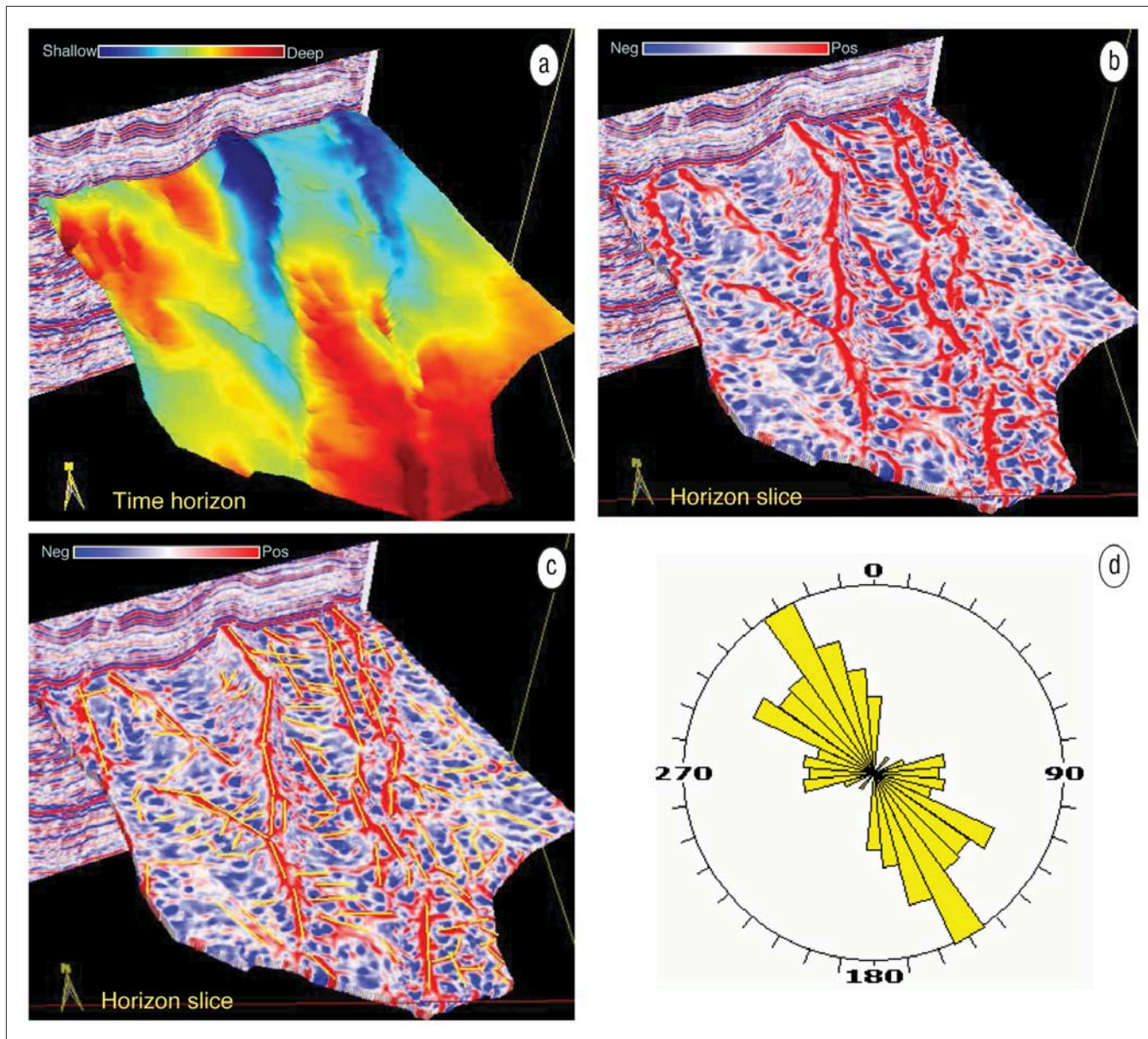
Figure 15. *(a) Time-structure map from a 3D seismic volume from British Columbia, and corresponding phantom horizon slices 30 ms below through (b), the most-positive curvature (long-wavelength). (c) Lineaments corresponding to the faults are marked as yellow lines. (d) Orientations of the marked lineaments (yellow) in (c) combined in the form of a rose diagram.*

picked horizon, while Figures 11c and d show the corresponding horizon slices through long-wavelength (α=0.25) and short-wavelength (α=0.80) volumetric computations of most-positive curvature. Notice the artifacts on the horizon-based most-positive curvature display (indicated with the blue and green arrows) that are largely absent in the two volumetric horizon slices.

Figure 12 shows the strat-cube displays of long-wavelength and short-wavelength versions of a fault/fracture system from Alberta. A strat-cube is a subvolume of seismic data or its attributes, either bounded by two horizons which may not necessarily be parallel or covering seismic data above and/or below a given horizon. The surface displayed is close to 1550 ms. Notice that the long-wavelength display gives the broad definition of such features, while the short-wavelength version depicts the finer definition of the individual lineaments.

Figure 13 shows another comparison of coherence and the most-positive long-wavelength and short-wavelength

curvature. The lineaments seen in the short-wavelength most-positive curvature images (Figure 13c) are more detailed than in the coherence (Figure 13a) and the long-wavelength most-positive curvature image (Figure 13b). All attribute interpretations on time and horizon slices should be validated through inspection of the vertical seismic data. Figure 14 shows enlarged views of the time slices from coherence, most-positive (both long-wavelength and high-resolution) and the long-wavelength most-negative curvature volumes intersecting a seismic inline. Notice that the red peaks (Figure 14b) on the fault lineaments (running almost NS) correlate with the upthrown signature on seismic. Similarly, the most-negative curvature time slice intersecting the seismic inline (Figure 14c) shows the downthrown edges (highlighted in blue) on both sides of the faults.

Curvature attributes for well-log calibration. Figure 15a shows a time surface and an intersecting seismic line from a 3D seismic volume from central-north British Columbia,

Canada. A number of faults can be seen on the vertical seismic section, and the main faults can be detected on the time surface as well. Figure 15b shows a horizon slice extracted from the most-positive curvature volume at a level 30 ms below the horizon in Figure 15a. The individual lineaments corresponding to the two main faults running N–S as well as their fracture offshoots have been tracked in yellow (Figure 15c). The orientations of these lineaments are displayed in a rose diagram (Figure 15d) which retains the color of the lineaments. This rose diagram can be compared to a similar diagram obtained from image wells logs to gain confidence in seismic-to-well calibration. Once a favorable match is obtained, the interpretation of fault/fracture orientations and the thicknesses over which they extend can be used with greater confidence for more quantitative reservoir analysis.

Conclusions. Curvature attributes provide important information above and beyond that derived from more commonly used seismic attributes. Being second-order derivative measures of surfaces, they are sensitive to noise. For time surfaces picked on noisy data, the noise problem can be addressed by iteratively running spatial filtering; for volume computation of attributes, structure-oriented filtering is satisfactory. Volume curvature attributes reveal valuable information on fracture orientation and density in zones where seismic horizons are not trackable. The orientations of the fault/fracture lineaments interpreted on curvature displays can be combined in rose diagrams, which in turn can be compared with similar diagrams obtained from image wells logs to gain confidence in seismic-to-well calibration.

Suggested reading. "Multispectral estimates of reflector curvature and rotation" by Al-Dossary and Marfurt (GEOPHYSICS, 2006). "Improving curvature analyses of deformed horizons using scale-dependent filtering techniques" by Bergbauer et al. (AAPG *Bulletin*, 2003). "Volume-based curvature analysis illuminates fracture orientations" by Blumentritt (AAPG Annual Convention, 2006). "Practical aspects of curvature computations from seismic horizons" by Chopra et al. (*SEG 2006 Expanded Abstracts*). "Curvature attribute applications to 3D seismic data" by Chopra and Marfurt (*TLE*, 2007). "Sunshading geophysical data using fractional order horizontal gradients" by Cooper and Cowans (*TLE*, 2003). "Facies and curvature-controlled 3D fracture models in a Cretaceous carbonate reservoir, Arabian Gulf" by Ericsson et al. (in *Faulting, fault sealing, and fluid flow in hydrocarbon reservoirs*, Geological Society Special Publication 147, 1988). "Validating seismic attributes: Beyond statistics" by Hart (*TLE*, 2002). "Improving seismic data for detailed structural interpretation" by Hesthammer (*TLE*, 1999). "Fast structural interpretation with structure-oriented filtering" by Hoecker and Fehmers (*TLE*, 2002). "Detection of zones of abnormal strains in structures using Gaussian curvature analysis" by Lisle (AAPG *Bulletin*, 1994). "Edge-preserving smoothing and applications" by Luo et al. (*TLE*, 2002). "Robust estimates of reflector dip and azimuth" by Marfurt (GEOPHYSICS, 2006). "Kinematic evolution and fracture prediction of the Valle Morado structure inferred from 3D seismic data, Salta province, northwest Argentina" by Massaferro et al. (AAPG *Bulletin*, 2003). "Curvature attributes and their application to 3D interpreted horizons" by Roberts (*First Break*, 2001). "Curvature attributes and seismic interpretation: Case studies from Argentina basins" by Sigismondi and Soldo (*TLE*, 2003). T|E

Corresponding author: schopra@arcis.com